51st AIAA Aerospace Sciences Meeting including the New Horizons Forum and Aerospace Exposition
07 - 10 January 2013, Grapevine (Dallas/Ft. Worth Region), Texas

AIAA 2013-0185

Preliminary Analysis of the Mars Science Laboratory's Entry Aerothermodynamic Environment and Thermal Protection System Performance

Milad Mahzari*and Robert D. Braun†
Georgia Institute of Technology, Atlanta, GA, 30332

Todd R. White‡
ERC Inc., Moffett Field, CA 94035

Deepak Bose§
NASA Ames Research Center, Moffett Field, CA 94035

The Mars Science Laboratory (MSL) entry vehicle successfully landed on the Martian surface on August 5, 2012. A phenolic impregnated carbon ablator heatshield was used to protect the spacecraft against the severe aeroheating environments of atmospheric entry. This heatshield was instrumented with a comprehensive set of pressure and temperature sensors. The objective of this paper is to present the thermal flight data returned and provide a preliminary post-flight analysis of MSL's aerothermal environment and heatshield thermal response. The flight temperature data are compared with the thermal response predictions by the same analytical models used in heatshield design. In addition to this direct comparison, a preliminary inverse analysis is performed where the time-dependent surface heating is estimated from flight-measured subsurface temperature data.

Nomenclature

$\mathbf{B}'$	Dimensionless surface blowing rate
C_H	Heat transfer coefficient = $\rho_e u_e C_h$
C_h	Stanton number for heat transfer
h	Enthalpy
H1	First-order Tikhonov regularization matrix
H_r	Total recovery enthalpy
J	Sensitivity matrix
$\dot{m}$	Surface blowing rate
M	Number of measurements
N	Number of discretized C_H points
p	Pressure
P	Vector of estimation parameters
q	Heat flux
Re_θ	Momentum thickness Reynolds number
S	Sum of square of errors (objective function)
t	Time
T	Temperature
T	Vector of direct problem outputs (FIAT predictions)
Y	Vector of measurements
α	Surface absorptivity

*Graduate Research Assistant, Guggenheim School of Aerospace Engineering, AIAA Student Member.
†David and Andrew Lewis Professor of Space Technology, Daniel Guggenheim School of Aerospace Engineering, AIAA Fellow.
‡Research Scientist, Aerothermodynamics Branch, AIAA Member.
§Senior Research Scientist, Aerothermodynamics Branch, AIAA Associate Fellow.

ϵ	Surface emissivity
μ	Regularization parameter
ρ	Density
σ	Stefan-Boltzmann constant

Subscript and superscripts

c	Char
$cond$	Conduction
e	Boundary layer edge
g	Pyrolysis gas
k	Iteration number
rad	Radiative
T	Transpose of a matrix
w	Material surface (wall)
∞	Freestream

I. Introduction

When spacecraft travel to other planets for surface missions, they are required to enter a planet's atmosphere at very high velocities to land on the surface. During entry, the interaction between the spacecraft and the planet's atmosphere dissipates more than 90% of the entry system's initial kinetic energy, mostly in the form of heat. The heatshield keeps the aeroshell interior safe from these extreme aeroheating environments. Since the heatshield is critical to mission success, the aerothermal environment and the Thermal Protection System (TPS) material response must be modeled accurately. However, there are substantial uncertainties associated with the analytical models that are currently used for predicting aeroheating and TPS response, such as heating augmentation due to turbulent transition and catalytic effects, TPS recession prediction and material properties.[1] These uncertainties have a significant effect on the TPS material selection and total mass, and therefore limit our ability to design more capable and robust Entry, Descent and Landing (EDL) systems.

Flight data can help engineers reduce these uncertainties to improve or validate the current computational tools. During the past decades, there have been entry missions that were equipped with instruments to collect aeroheating and TPS performance data. These missions were primarily in support of the Apollo and Shuttle programs and the majority of them occurred in the Earth atmosphere.[2] However, Mars has been and will continue to be a frequent destination in space exploration efforts. The need for Martian flight data is further justified because the experimental facilities on Earth are not capable of fully recreating Mars flight conditions. Mars Viking landers and Mars Pathfinder were the only missions that were equipped with instruments that returned heatshield data during their atmospheric entries. A few studies have been performed to analyze the data returned by these missions; however, due to the limited nature of these datasets it is difficult to make any general conclusions about Mars entry aerothermal modeling.[3–7]

Mars Science Laboratory (MSL) successfully landed on the Martian surface on August 5, 2012. The MSL aeroshell was a 4.5 m diameter spherically-blunted 70-degree half-angle cone with a triconic afterbody.[8] MSL's forebody heatshield was made of an ablative material called Phenolic Impregnated Carbon Ablators (PICA).[9] Based on the pre-flight aerothermal and heatshield analyses and mission mass allocations, a uniform PICA thickness of 1.25 in was used.[10–12] This heatshield was instrumented with a comprehensive set of pressure and temperature sensors called MSL Entry, Descent and Landing Instrumentation (MEDLI).[13] The aeroheating subsystem, called MEDLI Integrated Sensor Plug (MISP), provided subsurface temperature measurements of MSL's PICA heatshield at different locations and depths. The MEDLI dataset provided the first non-Earth entry aeroheating data since the Pathfinder mission, and more EDL data than all of the previous Mars missions combined.

The objective of this paper is to present the flight data returned by MISP sensors and provide a preliminary post-flight analysis of MSL's aerothermal environment and heatshield thermal response. First, some immediate observations regarding data range, quality and turbulent transition are discussed. Then, a direct analysis is performed to compare analytical model predictions with flight data. Computational Fluid Dynamics (CFD) simulations are performed using the NASA Ames code Data Parallel Line Relaxation (DPLR)[14]

to calculate the vehicle's aerothermal environment based on a pre-entry-simulated trajectory. The heatshield thermal response at MISP locations is calculated using the Fully Implicit Ablation and Thermal Response (FIAT) program.[15] These model predictions are compared with the flight thermocouple data. In addition to this direct analysis, a preliminary inverse analysis is also performed with the objective of reconstructing the vehicle's surface heating at MISP locations from flight data. Inverse methods are used to estimate the time-dependent surface heating profile that provides the best match between the thermocouple data and model predictions. See Ref. 16 for a complete overview of other MISP post-flight reconstruction efforts.

II. MISP Instrumentation

MEDLI consists of seven pressure ports and seven PICA plugs at different locations on the MSL heatshield. The suite consists of three subsystems: MISP temperature/isotherm sensors, MEADS pressure sensors, and Sensor Support Electronics (SSE). MISP sensors are installed into PICA plugs that are flush-mounted to the flight heatshield. The MISP plugs (Figure 1a, T labels) are strategically placed to cover a broad range of heat rate environments, while the MEADS locations (Figure 1a, P labels) are concentrated in the higher pressure and lower heat rate region near the stagnation point and the nose region.

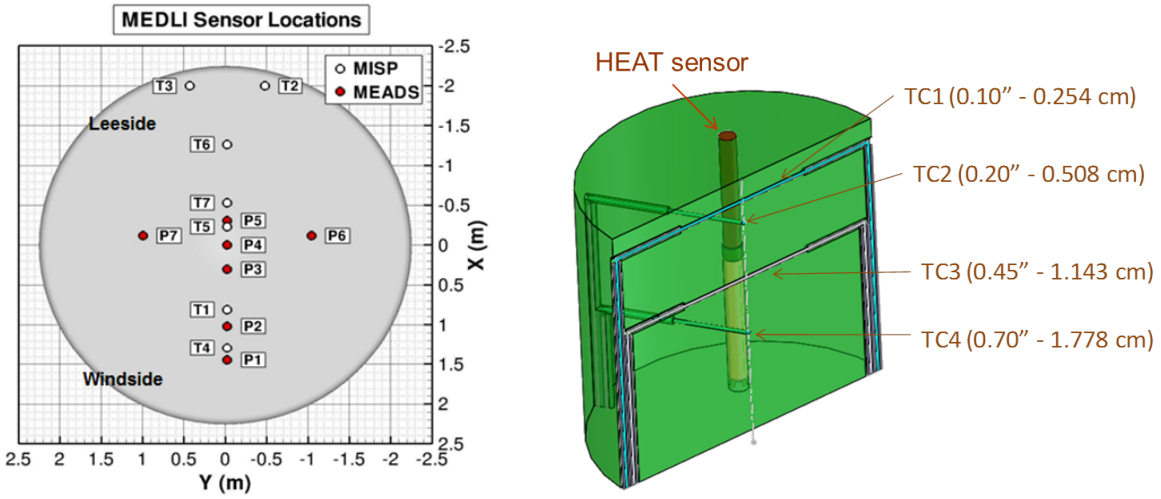

(a) Sensor Locations

(b) MISP Plug

Figure 1. Location of MEDLI sensors on MSL heatshield and schematic of MISP plug.[17]

Each MISP plug is 33 mm in diameter with a total depth of 20.3 mm, and contains four type-K U-shaped thermocouples. A schematic of a MISP plug is shown in Figure 1b. The thermocouples are at nominal design depths of 2.54, 5.08, 11.43, and 17.78 mm (0.10, 0.20, 0.45, 0.70 in) from the surface of the plug. The actual X-ray measured depths of each thermocouple are shown in Table 1. The top two thermocouples are intended primarily for aerothermodynamic reconstruction and are sampled at 8 Hz, while the two deeper thermocouples are primarily intended for material property reconstruction and are sampled at 1 or 2 Hz depending on the location. Data from TC3 and TC4 thermocouples in plugs 5 and 7 are not recorded because of data channel limitations.

Table 1. X-ray measured depths of MISP plugs thermocouples.

	Ideal (in)	Plug 1	Plug 2	Plug 3	Plug 4	Plug 5	Plug 6	Plug 7
TC1	0.100	0.104	0.106	0.103	0.097	0.099	0.108	0.094
TC2	0.200	0.200	0.203	0.193	0.212	0.192	0.203	0.193
TC3	0.450	0.452	0.456	0.456	0.446	0.461	0.460	0.442
TC4	0.700	0.704	0.700	0.693	0.706	0.703	0.695	0.699

Each MISP plug also contains an isotherm sensor called Hollow aErothermal Ablation and Temperature (HEAT).[18,19] HEAT is an improved version of a similar sensor that was used for the Galileo entry probe to

determine surface recession.[20] However, at the lower heat rates experienced during Martian entry, it is not expected to provide any information on recession. The sensor elements are conductive, so as the char layer-virgin material interface advances, these elements become shorter and the voltage output decreases. The HEAT sensor voltage measurements can be correlated with the sensor length which can then be correlated with char depth. The HEAT sensor is sampled at 8 Hz.

III. Observations from Flight Data

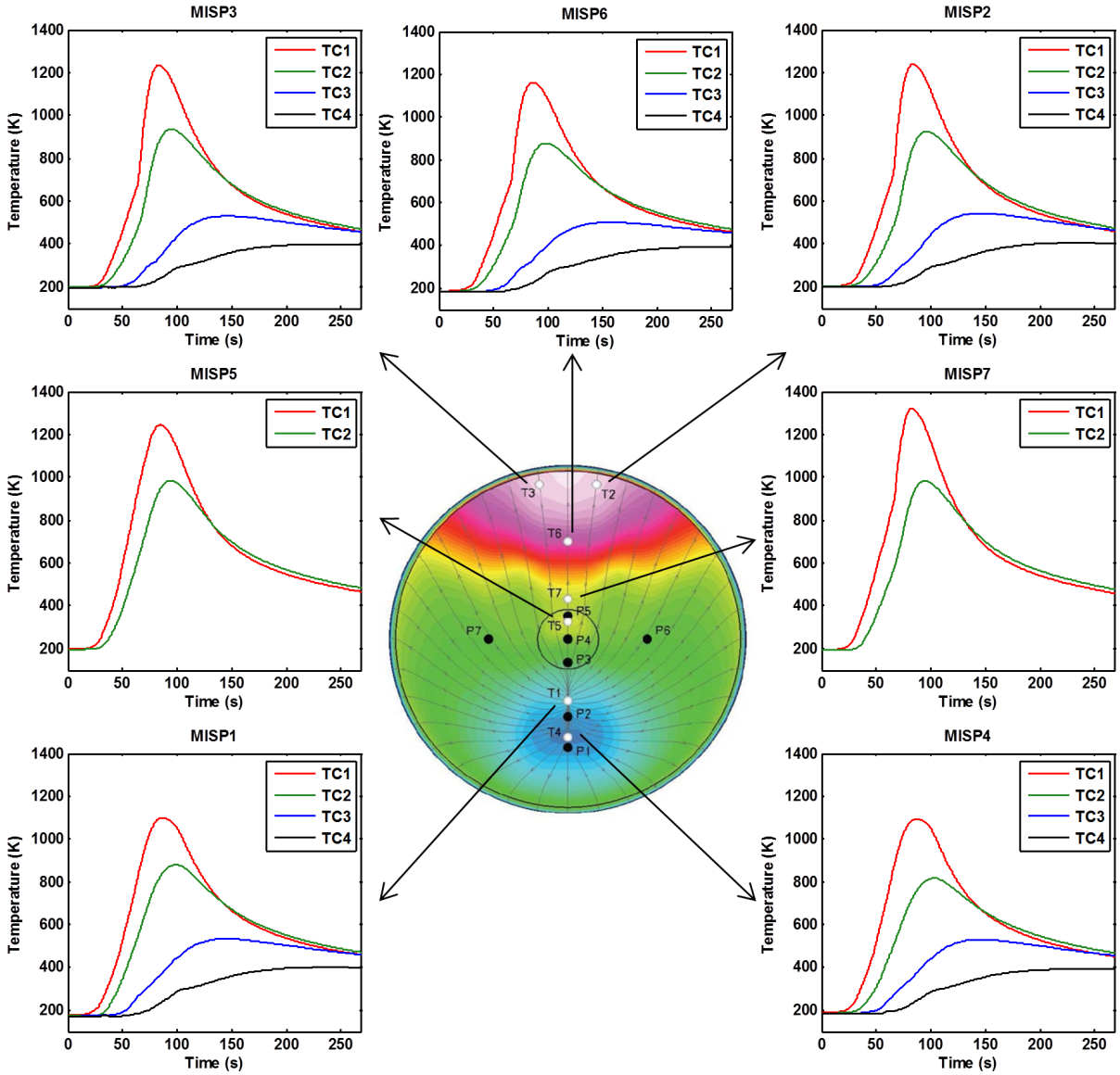

Figure 2. The MISP flight thermocouple data at different locations and depths on the heatshield.

The MEDLI data were recorded and stored successfully during the atmospheric entry. A limited part of the data was transmitted in real-time and the full dataset was received from the rover within a week after landing. The thermocouples behaved as expected and the data contained a low amount of noise. The HEAT sensor however did not behave as expected and the recorded transient data were very noisy. For this reason, the analysis of HEAT data is not pursued in this work. Figure 2 shows the MISP thermocouple flight data at all 7 plug locations. Time zero is the entry interface time corresponding to a spacecraft time (SCLK) of 397501714.953125 seconds. Thermocouple temperatures at this time ranged from 170 to 203 K depending

on TC depth and plug location.

Peak temperatures for the shallowest thermocouple (TC1) ranged from 1094 K at plug 4 to 1322 K at plug 7. Note that having the highest temperature does not necessarily mean that plug 7 experienced the highest heating as there is some variation in TC1 depth across different plugs (see Table 1). Peak temperatures for the deepest thermocouple (TC4) ranged from 393 K at plug 4 to 405 K at plug 7. Figure 3a shows TC1 temperature plotted as a function of time for all the plug locations. Examination of the TC1 temperature profile across different plugs informs us of the aeroheating environment distribution along the surface of the heatshield. We can see that up to 65 seconds, plug 5 has the highest temperature followed closely by plugs 7, 1 and 4, while plugs 2, 3 and 6 are at lower temperatures. This trend matches the surface heating distribution expected for laminar flow. After this time, we can clearly observe transition to turbulence for plugs 2, 3, 6, and 7 from the sudden slope change in the temperature data. Transition causes the TC1 temperature at these plugs to rise more rapidly and eventually reach higher peak values. Specifically, since plug 7 was already at a high level of laminar heating, its temperature increased to be the highest peak after transition.

Figure 3b illustrates the TC1 temperature rise rate as a function of time for these plugs. Sharp increases can be observed in the temperature rise rates during the 63-66 s time period. Plug 3 becomes turbulent around 64 seconds, followed by plug 2 at 65 seconds, and plugs 6 and 7 at 66 seconds. It should be noted that these transition times are based on the slope changes observed in the subsurface thermocouple data. In-depth temperature response lags somewhat behind any changes in the surface heating; therefore, the actual surface turbulent transition times are within 1-2 seconds of the numbers reported here. In the inverse analysis section, we will provide a better estimate of transition time based on surface heating reconstruction results. The transition front moved very quickly from plugs 2 and 3 at the shoulder to plugs 6 and 7. Pre-flight predictions indicated transitions times of 56, 58, and 70 seconds for plugs 2 (3), 6, and 7 respectively. These predictions are based on a smooth wall momentum thickness Reynolds number threshold of 250. It is currently believed that the observed quick motion of the transition front is due to roughness-induced transition. See Ref. 16 for more information on this topic.

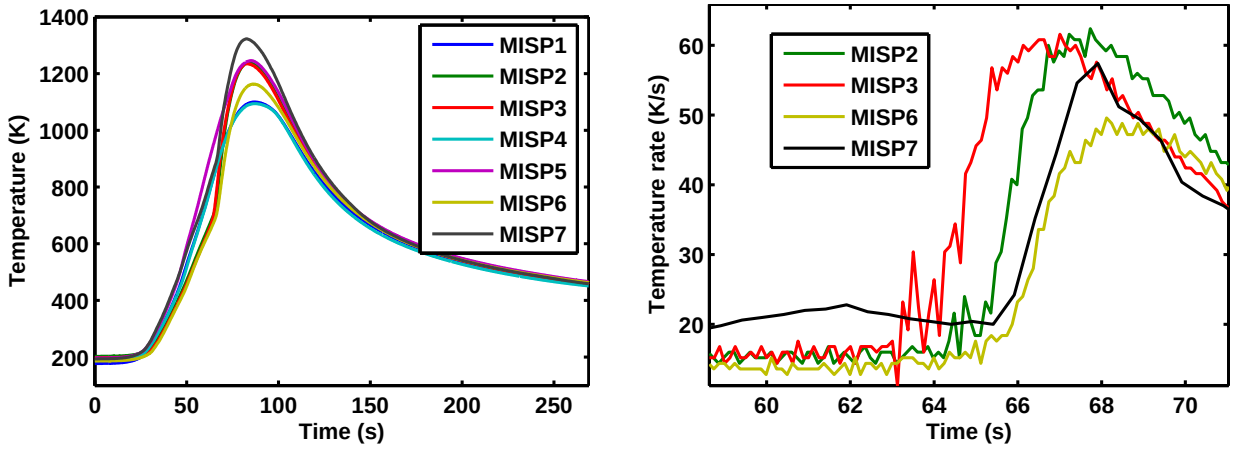

(a) TC1 Temperature

(b) TC1 Temperature Rise Rate

Figure 3. Transition to turbulence can be seen from TC1 data for plugs 2, 3, 6 and 7.

Turbulent heating augmentation can be estimated by comparing the pre-rise and post-rise temperature rates. Table 2 shows the pre-rise and post-rise temperature rates over a two-second period for the four plugs that experienced turbulent transition. The ratio of these rates is an approximate indication of the turbulent heating augmentation level. Turbulent augmentation is expected to increase as the running length from the stagnation point to the plug increases. The results in Table 2 follow the expected trend. It should be noted that the calculated values are for in-depth temperature rates which are damped compared with surface heating. Additionally, other surface phenomena such as reradiation can affect this temperature rate. Therefore, the values in this table should not be taken as exact surface heating augmentations.

In Figure 4, we can see that there is an unexpected slope change ("hump") in the temperature profile for the deeper thermocouples (TC3-4) at plug 2. The hump happens in the 250-300 K temperature range. This trend is observed consistently for all plug locations. Similar behavior has also been seen in the MISP

Table 2. Turbulent temperature augmentation over a two-second period derived from TC1 temperature rates.

	Plug 2	Plug3	Plug 6	Plug 7
$(dT/dt)_{pre}$ (K/s)	16	16	14	21
$(dT/dt)_{post}$ (K/s)	61	60	48	56
Temperature augmentation (ratio)	3.81	3.75	3.43	2.80

qualification arcjet dataset, arcjet testing for some other materials than PICA, and also for Mars Pathfinder bondline thermocouples flight data. This phenomenon is not well understood at present, but is believed to be associated with some type of material- or instrument-related process. Current analysis tools are not able to model this behavior; therefore, we should not expect a match between the data and model predictions for this part of the data.

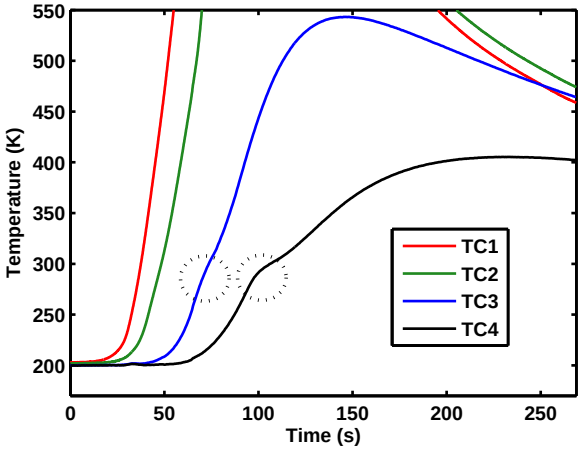

Figure 4. The "hump" observed in TC3 and TC4 data for plug 2 (seen also for other plugs).

IV. Direct Analysis

The purpose of the direct analysis is to perform an updated analysis of the MSL heating environment and TPS material response using the computational models that were employed in the design process. These model predictions are then compared with the flight data.

IV.A. Aerothermal Environment Prediction

The best-estimate trajectory based on the flight Inertial Measurement Unit (IMU) and MEADS data was not available in time for this study. Therefore, a pre-entry-simulated trajectory based on the latest orbital determination estimates is used in this work. This trajectory is known as OD229 and was generated using the Program to Optimize Simulated Trajectories II (POST2).[21] Figure 5 shows plots for the altitude as a function of velocity and velocity as a function of time for the OD229 trajectory. This trajectory has been compared with early versions of the MSL's best-estimate trajectory[22] and there is good agreement between the two during the hypersonic region. Any differences between the two trajectories are expected to have minor impact on aerothermal modeling.

In order to predict the vehicle's aeroheating environment, CFD simulations are performed based on this trajectory using DPLR. DPLR is a modern, parallel, structured non-equilibrium Navier-Stokes flow solver developed and maintained at NASA Ames Research Center.[14] The code employs a modified Steger-Warming flux-splitting scheme for higher-order differencing of the inviscid fluxes, and is used here with 2^{nd} order spatial accuracy and to steady-state 1^{st} order in time. The flow around the heatshield is modeled as thermochemical non-equilibrium flow, using the Mitcheltree and Gnoffo 8-species 12-reactions Mars model (CO_2, CO, N_2, O_2, NO, C, N, and O).[23] The Mars atmosphere is modeled as 97% CO_2 and 3% N_2 by mass. The TPS surface is modeled as an unblown non-slip radiative equilibrium wall with constant emissivity ($\epsilon = 0.85$) and the

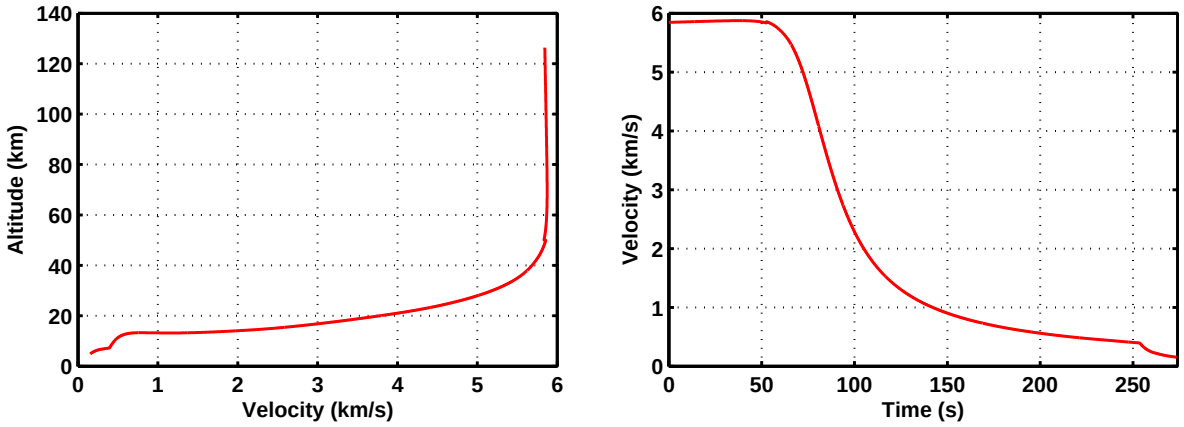

Figure 5. MSL entry trajectory (OD229) used in this analysis.

Mitcheltree and Gnoffo surface catalycity model.[24] This catalycity model assumes maximum recombination of CO_2 via the Eley-Rideal mechanism. Species diffusion is modeled using self-consistent effective binary diffusion (SCEBD).[25] Turbulent flow is simulated with the Baldwin-Lomax algebraic model.[26]

CFD calculations are performed along the entry trajectory from 40 to 90 seconds, at two-to-five second intervals. Surface properties for material response simulations are extracted from the CFD solutions at each MISP location. These quantities are then fitted in time with tight monotonic cubic splines, and provided as boundary condition inputs to the FIAT material response code at quarter-second intervals. In this direct approach, surface heating for the periods before 25 seconds and after 115 seconds is assumed to be zero. Figure 6 shows the CFD-predicted surface heat rate and pressure as functions of time at all MISP plugs for the laminar, fully turbulent and transitional solutions. CFD environments for MISP3 are identical to MISP2 and are not shown here. These predicted surface heat rates are lower than the design values reported in Ref. 10. This is due to the fact that conservative approaches such as fully turbulent flow, supercatalytic wall and roughness augmentation are employed for design environments. For TPS response analysis, the transitional solutions shown in Figure 6 are applied. The transition front is modeled such that laminar solutions are used for $Re_\theta < 200$, and a linearly varying transition front is imposed for Re_θ of 200 to 250. At plug 2 and plug 3, the fully-turbulent heating value is reached quickly. However, for plugs 6 and 7, the transitional solution heating does not reach fully turbulent levels until well after the peak heat pulse.

IV.B. Thermal Response Prediction & Comparison with Flight Data

For an ablative material, surface heat rate is not a direct input to FIAT. Surface heating is modeled with a surface energy balance equation which represents many physical phenomena that occur at the surface of an ablative material. This equation is:

$$C_H(H_r - h_w) + \dot{m}_g h_g + \dot{m}_c h_c - (\dot{m}_c + \dot{m}_g)\, h_w + \alpha_w q_{rad} - \sigma \epsilon_w (T_w^4 - T_\infty^4) - q_{cond} = 0 \qquad (1)$$

The first term in the equation represents the sensible convective heat rate. The sum of the second, third and fourth terms defines the total chemical energy at the surface due to the ablation products and pyrolysis gas. The fifth and sixth terms are the incoming radiative heat rate absorbed by the material and the reradiation to the environment. The last term in Eq. (1) represents the rate of heat conduction into the TPS material. CFD models calculate the convective heat rate at the surface typically based on a radiative equilibrium wall assumption and a given surface catalycity model ignoring ablation and pyrolysis effects and heat conduction into the TPS. Based on these assumptions, the total recovery enthalpy, H_r, and wall enthalpy, h_w, can be derived. Knowing these values and the convective heat rate, the surface heat transfer coefficient, C_H, is calculated. C_H, H_r, surface pressure, and the blowing reduction parameter are input to FIAT as functions of time. It should be noted that the CFD heat transfer coefficient values are unblown, and FIAT corrects the input C_H for heating reduction due to pyrolysis gas blowing.[15]

The above equation is solved in FIAT using its own wall chemistry model that accounts for ablation and pyrolysis. Pre-calculated equilibrium wall chemistry solutions (B' tables) are input to FIAT for a given material and the surface energy balance is solved iteratively using the heating inputs from CFD and the

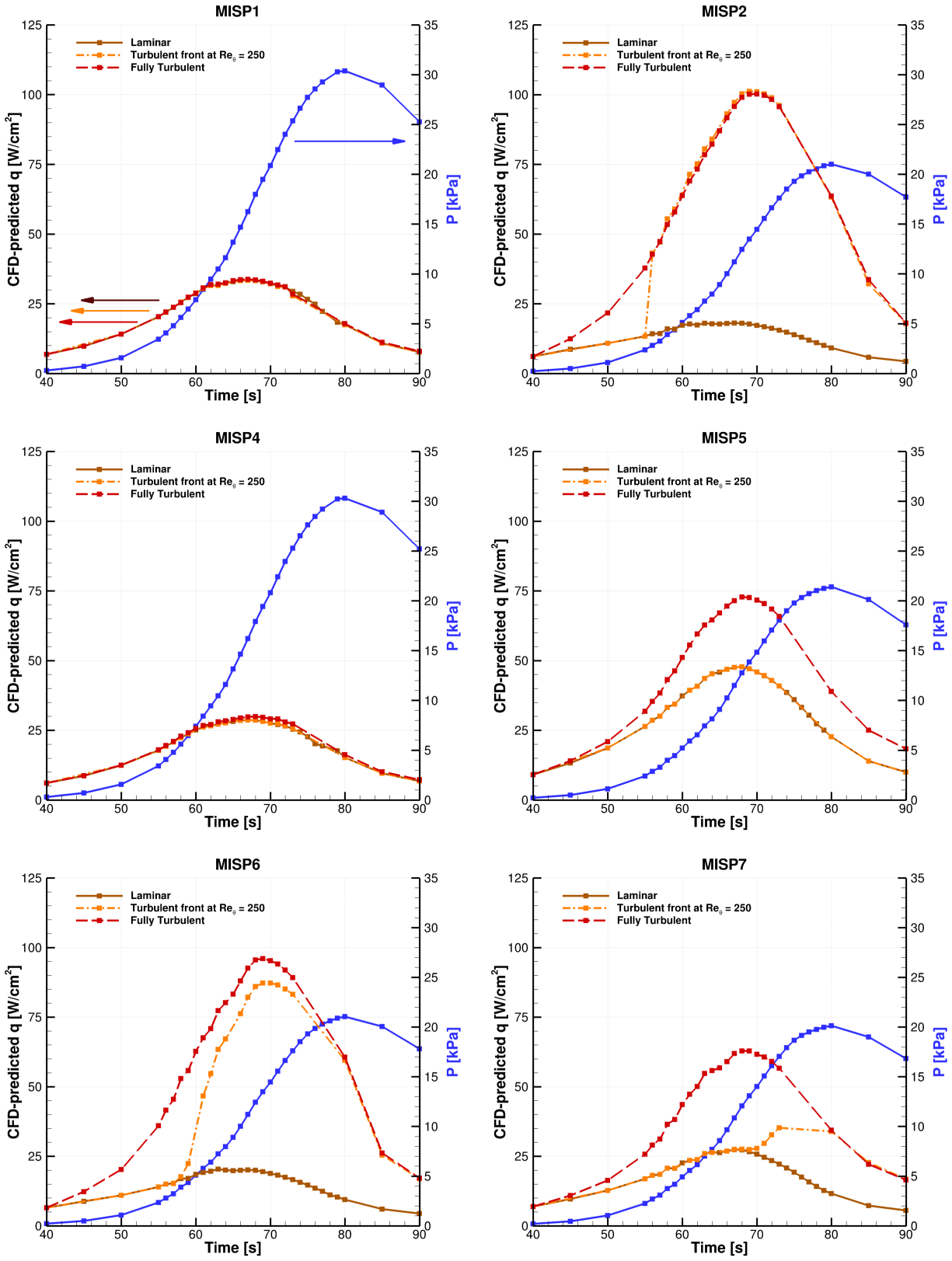

Figure 6. MISP CFD-predicted environments on OD229 trajectory.

B' tables. This results in an inconsistency between the surface chemistry solutions of the CFD and FIAT calculations which results in different wall enthalpies and temperatures. Different wall chemistries, heating reduction due to pyrolysis gas blowing, and conduction into TPS mean that the surface heat rate calculated by FIAT differs from the values reported by CFD tools for the same environments. The surface heat rate derived from FIAT solutions is typically taken to be the sum of the first four terms in Eq. (1) (all the terms except radiation, reradiation and conduction terms). This difference should be taken into account because the FIAT-calculated heat rate values reported in this paper are typically lower than their corresponding CFD values. Figure 7 shows the FIAT surface heat rate for all the MISP plugs corresponding to the transitional heating environments calculated by DPLR and shown in Figure 6.

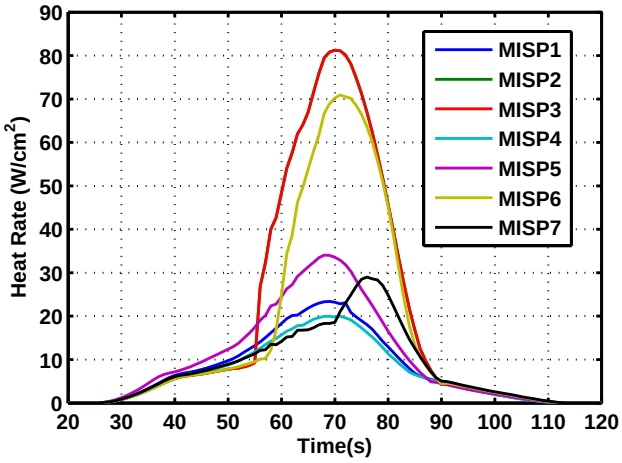

Figure 7. The surface heat rate for all MISP plugs calculated with FIAT.

For the following FIAT simulations, radiative heating is assumed to be negligible. Reradiation is modeled to an environment with an effective temperature of 180 K. A manual grid is employed to specify the initial temperature distribution of the PICA block according to the flight data initial temperatures. The TC depths are taken from the X-ray measurements shown in Table 1. The blowing reduction parameter is assumed to be 0.5 for laminar flow and 0.3 for turbulent flow. PICA material model version 3.3 is used in this analysis. In the following plots, FIAT temperature predictions at all plugs are shown against the flight data. It should be noted that while the temperature predictions are shown at all TC depths for the sake of completeness, the focus will be mainly on how the top thermocouple results compare as it is the closest to the surface and most sensitive to surface heating. The deeper TC data will be affected by the uncertainty in the surface heating; therefore, comparison of those data with predictions is not a good indication of the accuracy of the in-depth material response model. More representative comparisons for the deeper TC data are presented in the next section using the TC driver approach.

Figure 8 shows the FIAT temperature predictions compared with flight data at plugs 1 and 4. These plugs are on the heatshield windside and close to the stagnation point. We can see that the analytical models underpredict the flight data. Possible causes for this difference could be radiative heating or low levels of flow turbulence due to pyrolysis gas injection. Additionally, arcjet tests have shown that molten Silica from the RTV bonding used around the plugs can flow on the surface of a plug and result in lower emissivity and therefore lower reradiation.

Figure 9 shows the comparison with flight data for plugs 2 and 3. These plugs are close to the leeside shoulder. Being farthest from stagnation point, they were expected to see the highest heating augmentations due to turbulent transition. We can see that model predictions significantly overpredict the flight data for these plugs. This is due to the fact that transition to turbulence happened much later than expected and for that reason the surface heating did not have as much time to increase. Therefore, the turbulent temperature augmentation at these locations was less than model predictions. We can also see in FIAT predictions that TC1 was expected to burn out because of recession. This did not occur in flight because of the lower than expected heating levels and also possibly because the equilibrium models used in FIAT for gas/surface interactions are known to overpredict recession at the range of heat rates experienced by the MSL vehicle.[27] The only information that we can obtain from flight data regarding recession is that it was less than TC1

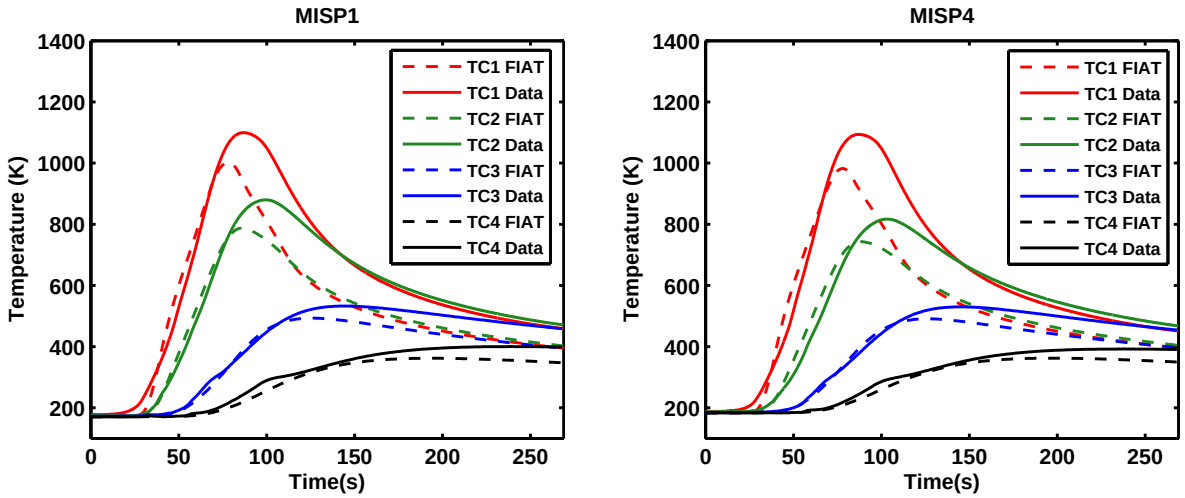

Figure 8. FIAT predictions compared with flight data for plugs 1 and 4.

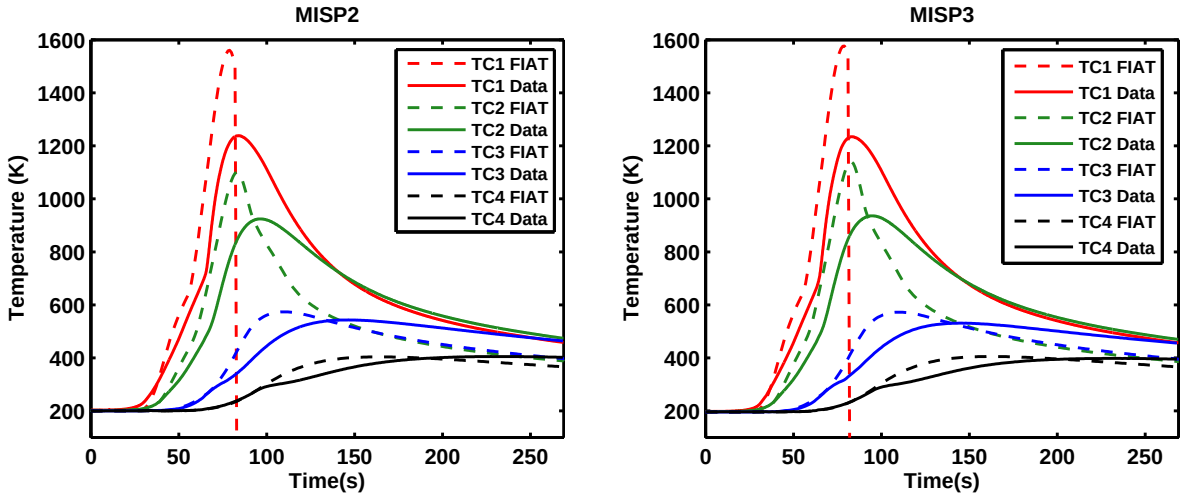

Figure 9. FIAT predictions compared with flight data for plugs 2 and 3.

depth ($\simeq$ 0.1 inch) for all plugs.

Model predictions and flight data are compared in Figure 10 for plugs 5 and 7. These plugs are close to the heatshield apex. Same observations as plugs 1 and 4 can be made for plug 5. Laminar heating is underpredicted, possibly because of the lower reradiation due to lower surface emissivity caused by Silica flow. Plug 7 experienced higher than expected heating because of earlier transition to turbulence as compared with CFD predictions. In CFD environments, transition happens quite late in the trajectory for plug 7; therefore, heating does not rise to very high levels.

Figure 11 shows the comparison for plug 6. Similar observations as for plugs 2 and 3 can be made. Based on CFD environments, transition to turbulence was expected to happen earlier in the trajectory (58 seconds). However, since flight transition happened later, the temperature augmentation was not as much as the model predictions.

One important observation that was made in the comparisons between the data and model predictions for all plugs was that the temperature pulse in the data was wider than model predictions. In other words, analytical models predict TC1 to cool down at a faster rate than flight. This could be due to many reasons such as higher post-peak surface heating, lower surface emissivity, uncertainty in char material properties at high temperatures, or a combination of all possibilities. Adjustments of some of these parameters result in a slightly better agreement with the data, although not a significant one. Further sensitivity studies need to be performed in future to determine the most probable cause of this pulse-width disagreement.

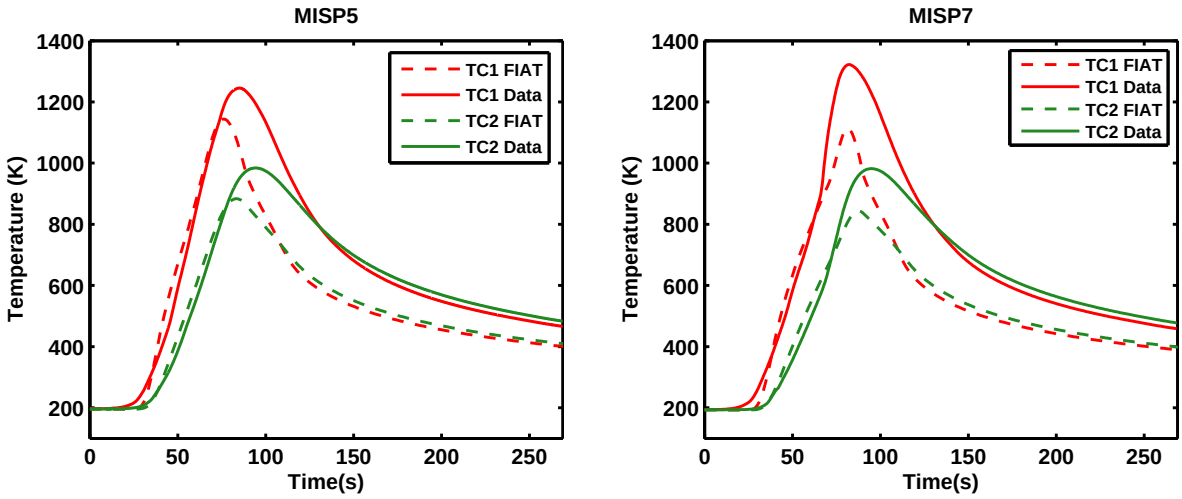

Figure 10. FIAT predictions compared with flight data for plugs 5 and 7.

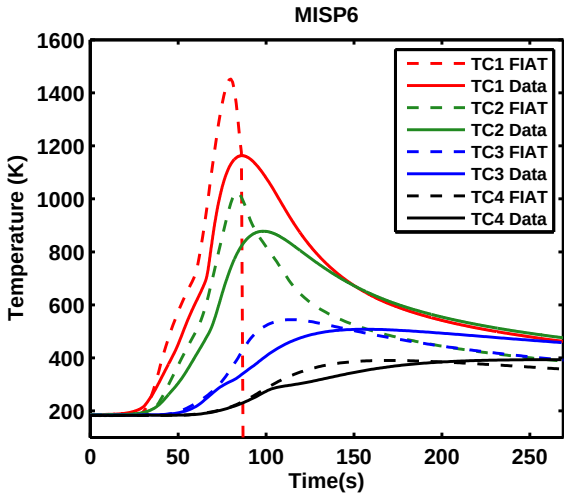

Figure 11. FIAT predictions compared with flight data for plug 6.

IV.C. TC Driver Analysis

The data from the shallowest thermocouple (TC1) can be used as a true boundary condition and the thermal response for the material beneath that thermocouple can be calculated using FIAT. This TC driver approach effectively decouples the in-depth heat conduction from the surface heating conditions. This allows us to examine the performance of the in-depth material model without being affected by the uncertainty of surface heating. Figure 12 shows the TC driver analysis for plugs 1 and 2. FIAT temperature predictions for TC2-4 are compared with flight data. We can observe that in both cases there is a good agreement between FIAT and TC2 flight data. However, TC3 and TC4 data do not match FIAT predictions as well. This trend is seen in all plugs. The slope changes seen in these TC data ("hump") can explain the initial part of the difference. Other possible explanations include virgin material property uncertainty and multi-dimensional effects. Further examination of the TC driver problem and material property estimation will be pursued in future. Overall, it seems that the material model is conservative in predicting in-depth temperature.

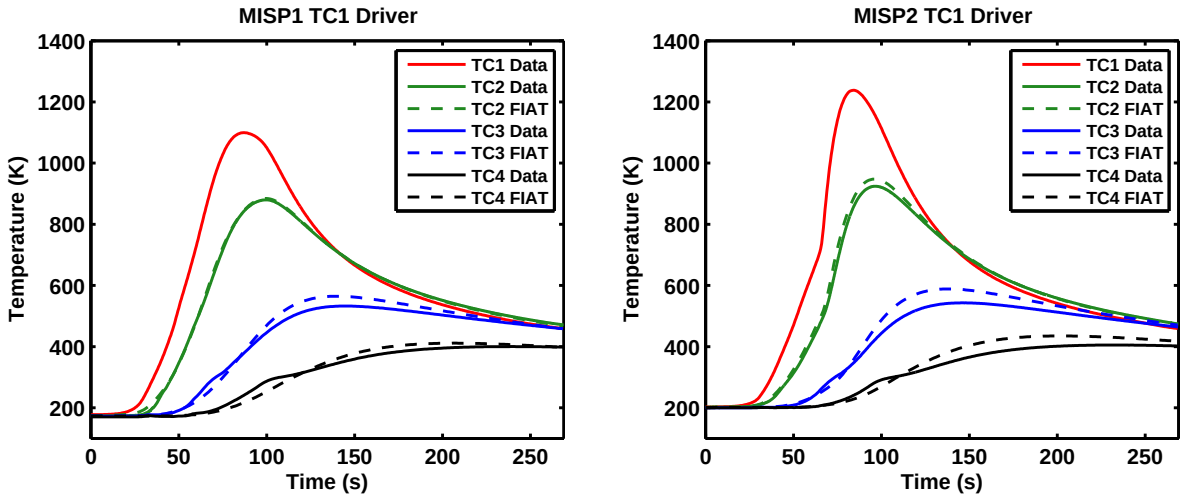

Figure 12. In-depth material response analysis using the TC driver approach for plugs 1 and 2.

V. Inverse Analysis

V.A. Methodology

The goal of inverse analysis is to reconstruct the vehicle's surface heating at the MISP locations from flight data. Inverse problems are encountered in many science and engineering applications. In the heat transfer field, these problems often involve the estimation of a boundary condition such as surface heating or temperature, or the estimation of model parameters such as material thermophysical properties.[28–30] Estimation of time-dependent surface heating belongs to the class of function estimation problems, as they require the identification of many points in time. Inverse methods attempt to estimate the surface heating by minimizing the difference between analytical model predictions and experimental measurements. Two classes of methods are typically used for surface heating estimation: whole-time domain methods and sequential methods. Whole-time domain methods iteratively estimate the entire heating profile at the same time using the entire measurement range, while sequential methods estimate the surface heating at a given time using a limited subset of the measurements and proceed sequentially in time. Sequential methods can be more efficient if set up properly; however, whole-time domain methods are typically more stable and can be more easily integrated with FIAT. For these reasons, we use whole-time domain methods in this work.

In this analysis we will use the shallowest thermocouple data (TC1) as it is the most sensitive to surface heating and least affected by subsurface material property uncertainty. The authors have previously developed methods for similar applications and applied them to MSL simulated data[31] and Mars Pathfinder flight data.[7] As explained earlier in Eq. (1), surface heating is modeled in FIAT using a detailed surface energy balance equation which includes a convective term, pyrolysis and ablation terms, radiation and reradiation terms, and conduction into the TPS. Many of the parameters in this equation can affect the subsurface thermocouple temperature and the surface heating estimate. Some of these parameters are inputs to FIAT while others are calculated internally by FIAT. While it is desirable to have an accurate knowledge of all these terms, they are not all directly observable from the flight data and any attempt to simultaneously estimate multiple parameters leads to non-unique solutions. Therefore, a parameter has to be selected for inverse estimation while other parameters are fixed or calculated internally.

The approach that has been used in previous work is to estimate the time-dependent surface heat transfer coefficient, C_H. In this approach, we assume that the CFD recovery enthalpy and pressure predictions are accurate and we allow FIAT to calculate the in-depth pyrolysis and wall chemistry according to the equilibrium B' tables. We also assume that the reradiation term calculated by FIAT is accurate. The goal is to estimate the C_H profile that provides the best match between the flight data and FIAT predictions. Since C_H is a time-dependent parameter, it is discretized in time to one-second control points for inverse estimation. Once the the time-dependent C_H profile is estimated, the corresponding heat rate profile can be calculated based on FIAT's surface energy balance. The FIAT heat rate reported in this paper is the sum of the first four terms in Eq. (1) (convective and chemical terms).

The estimation is done by iterative minimization of an objective function S (ordinary least-squares), which is the sum of the squares of differences between the thermocouple measurements and the corresponding FIAT temperature predictions. The set of parameters that minimize this function is the solution of the inverse problem. The ordinary least-squares objective function is shown in Eq. (2) in both standard and matrix forms:

$$S\left(\mathbf{P}\right) = \left[\mathbf{Y} - \mathbf{T}\left(\mathbf{P}\right)\right]^T \left[\mathbf{Y} - \mathbf{T}\left(\mathbf{P}\right)\right] = \sum_{i=1}^{M} \left(Y_i - T_i\right)^2 \tag{2}$$

$\mathbf{P}$ is the vector of parameters being estimated (discretized C_H time history), $\mathbf{Y}$ is the vector of TC1 temperature measurements, and $\mathbf{T}$ is the corresponding vector of temperature predictions by FIAT. The Gauss-Newton[29,32] method is used to perform the minimization of the objective function. This method is widely used to solve nonlinear least squares problems. It is a modification of Newton's method which does not require the knowledge of second derivatives. The search algorithm for this method is developed by deriving the gradient of the above equation, linearizing the vector of predicted temperatures $\mathbf{T}(\mathbf{P})$ with a Taylor series expansion around the current solution $\mathbf{P}^k$ and setting the gradient of S to zero. The expression can be rewritten to derive the change in parameters $\Delta\mathbf{P}$ required to minimize S:

$$\mathbf{J^{k^T}J^k\Delta P^k} = \mathbf{J^{k^T}}\left[\mathbf{Y} - \mathbf{T}\left(\mathbf{P^k}\right)\right] \tag{3}$$

where $\mathbf{J}$ is the Jacobian matrix of the first partial derivative of the predicted TC temperatures with respect to the estimation parameters (discretized points along the C_H profile):

$$\mathbf{J} = \begin{bmatrix} \frac{\partial T_1}{\partial P_1} & \cdots & \frac{\partial T_1}{\partial P_N} \\ \vdots & \ddots & \vdots \\ \frac{\partial T_M}{\partial P_1} & \cdots & \frac{\partial T_M}{\partial P_N} \end{bmatrix} \tag{4}$$

where M is the number of measurements and N is the number of estimation parameters. The calculation of this Jacobian matrix is computationally expensive because its numerical approximation by finite differencing requires N solutions of the direct problem (FIAT). This procedure is continued until a stopping criterion is reached.

Inverse problems are mathematically ill-posed meaning that conditions of solution existence, uniqueness and stability are not guaranteed. These problems can be unstable in the presence of errors or when large number of parameters are estimated. This can result in significant oscillations that lead to inaccurate estimation results. Regularization approaches are used in conjunction with the minimization scheme to make the problem better posed and more stable. Regularization has a smoothing effect on the parameter estimates. Russian mathematician Andrey Tikhonov devised a procedure for the regularization of ill-posed problems.[33] His technique involves the addition of a penalty function to the ordinary least-squares objective function to alleviate oscillations in the solution. The penalty function added is the sum of squares of differences between the consecutive C_H values. Equations (2) and (3) need to be modified accordingly:

$$S = \left[\mathbf{Y} - \mathbf{T}\right]^T \left[\mathbf{Y} - \mathbf{T}\right] + \mu \left[\mathbf{H1} \times \mathbf{P}\right]^T \left[\mathbf{H1} \times \mathbf{P}\right] = \sum_{i=1}^{M} \left(Y_i - T_i\right)^2 + \mu \sum_{j=1}^{N-1} \left(P_{j+1} - P_j\right)^2 \tag{5}$$

$$\left[\mathbf{J^TJ} + \mu\mathbf{H1^TH1}\right]\Delta\mathbf{P} = \mathbf{J^T}\left[\mathbf{Y} - \mathbf{T}\right] \tag{6}$$

$$\mathbf{H1} = \begin{bmatrix} -1 & 1 & 0 & \cdots & 0 \\ 0 & -1 & 1 & \cdots & 0 \\ \vdots & \ddots & \ddots & \ddots & \vdots \\ 0 & \cdots & 0 & -1 & 1 \\ 0 & 0 & \cdots & 0 & 0 \end{bmatrix} \tag{7}$$

Small values of μ ensure rapid minimization of the ordinary least-squares function, but could result in large oscillations in the C_H profile. Larger values of μ reduce oscillations, but slow down the minimization of the objective function. In this investigation, a small value of μ is used initially and increased until the

obtained estimate appears satisfactory and the degree of oscillation is reduced sufficiently. Qualitatively, a good solution is a solution that traces through the unregularized oscillatory solution. It should be noted that while regularization helps with obtaining a smooth solution it also smooths out sharp changes in the heating profile. Therefore, for determination of turbulent transition time, solutions with low levels of regularization are preferred. The MISP data contained very little noise; therefore, only a low level of regularization is needed.

It should be noted that the C_H estimation approach used here has some limitations. The authors realize how other surface energy balance terms can affect the subsurface temperature and further analyses to study such cases will be pursued in future work. Additionally, the slower post-peak temperature cooling rate observed in the data can not be matched using this C_H estimation approach. The recovery enthalpy becomes negative around peak temperature time, making the convective heating term negative. In order to match the higher post-peak temperatures, the estimator attempts to increase C_H to very high values to increase the chemical heating contribution while not significantly affecting conduction into the TPS due to the fact that the negative convective term also increases. In other words, TC1 temperature loses its sensitivity to C_H adjustment around the peak temperature time. Therefore in this work, inverse estimation is performed up to the peak temperature time ($\approx$ 85 seconds). Since subsurface temperature response lags the surface heating, this approach ensures that the peak heating point is estimated.

V.B. Reconstruction Results

Figures 13 and 14 illustrate the estimation results for plug 7. TC1 temperature is plotted for both the direct and estimated environments in Figure 13a. The blue line corresponds to estimated environments while the red line corresponds to the surface heating based on CFD predictions. The black symbols show the flight TC1 data. We can see that FIAT predictions match the data almost identically after inverse estimation of the surface heating. TC1 temperature residuals with respect to flight data are shown in Figure 13b. Almost a perfect match with the data is achieved and residuals are reduced to within 1 K after estimation.

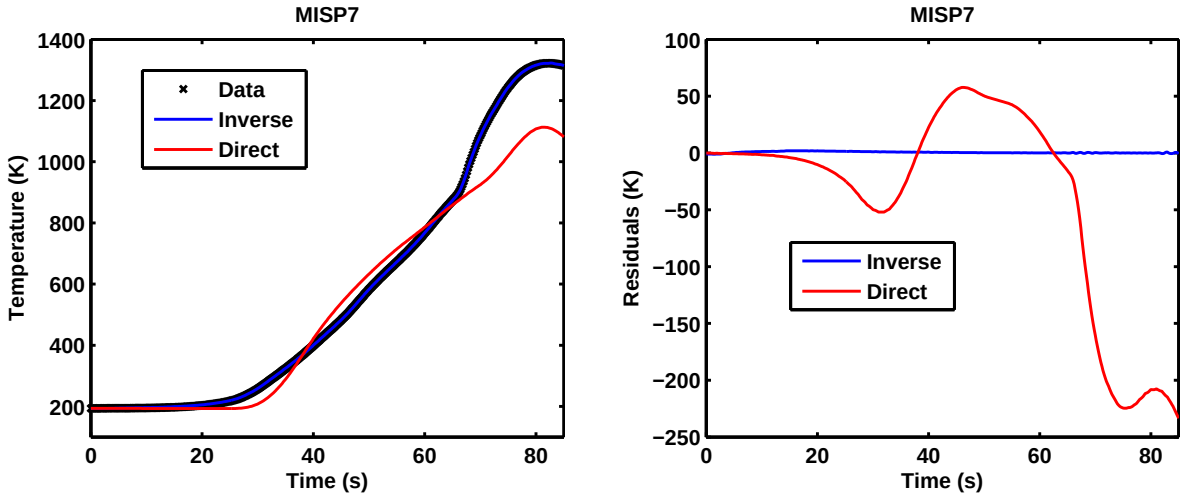

(a) TC1 Temperature

(b) Temperature Residuals w.r.t Flight Data

Figure 13. TC1 temperature and residual with respect to data for plug 7 reconstruction.

Figure 14 shows the inversely estimated surface heat rate profile compared with the direct FIAT heat rates based on CFD nominal predictions for plug 7. As discussed before, turbulent transition happens much earlier than CFD predictions for this plug and the estimated surface heat rate increases significantly. We can also observe that for about 10 seconds before transition, laminar heating is higher than CFD predictions.

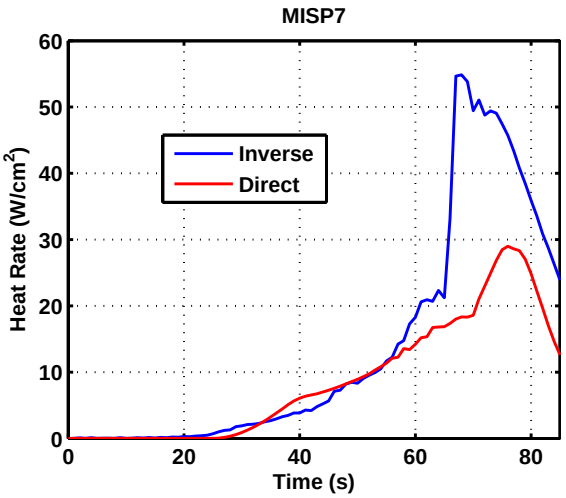

Figure 14. Comparison of the inversely estimated and direct FIAT heating environments for plug 7.

Comparisons of TC1 temperature profiles and residuals are not shown for the rest of the plugs. However, similar performances are achieved and almost a perfect match between the data and FIAT predictions is reached in all cases through inverse estimation. Figure 15 shows the estimated surface heating profile compared with the direct FIAT heating profile based on CFD predictions for plugs 2 and 3. We can see that transition to turbulence happened a little before peak heating and the surface heating increased very rapidly. In general, there is not a good agreement between the shape and magnitude of the estimated heating profile and the CFD predictions at these plugs. CFD predictions were greatly conservative. Plug 3 experienced lower peak heating and slightly lower turbulent augmentation than plug 2 even though they were in symmetric positions. This could be due to oscillations in sideslip angle or a local effect.

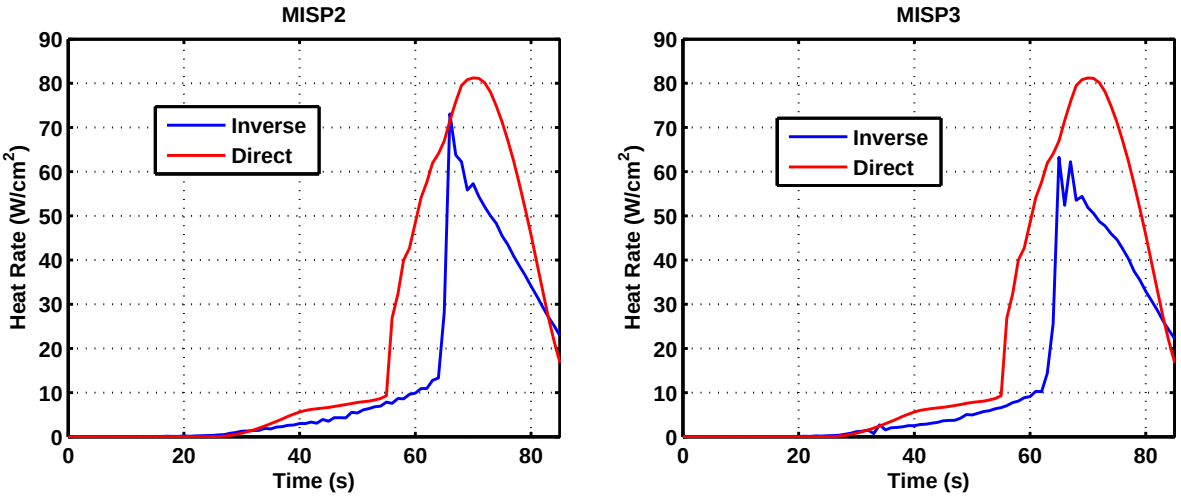

Figure 15. Comparison of the estimated and direct FIAT heating environments for plugs 2 and 3.

Figure 16 shows the same comparison for plugs 5 and 6. Observations for plugs 2 and 3 apply similarly to plug 6. Plug 5 remained laminar for the entire trajectory. The estimated surface heating is slightly higher than CFD predicted values and the peak heat rate happens a little later than CFD predictions. Estimation results for plug 1 and 4 are shown in Figure 17. Estimated heating profile reaches higher values compared with the direct FIAT surface heating based on CFD predictions. Similar to plug 5, the estimated peak heat rate happens a little later than CFD predictions. The shapes of the estimated heating profiles are slightly different from CFD predictions. Laminar heating predictions are higher than estimated values from 30 to 60 seconds and lower after 60 seconds.

Table 3 shows a comparison of the estimated peak heat rates (inverse) and FIAT peak heat rates based

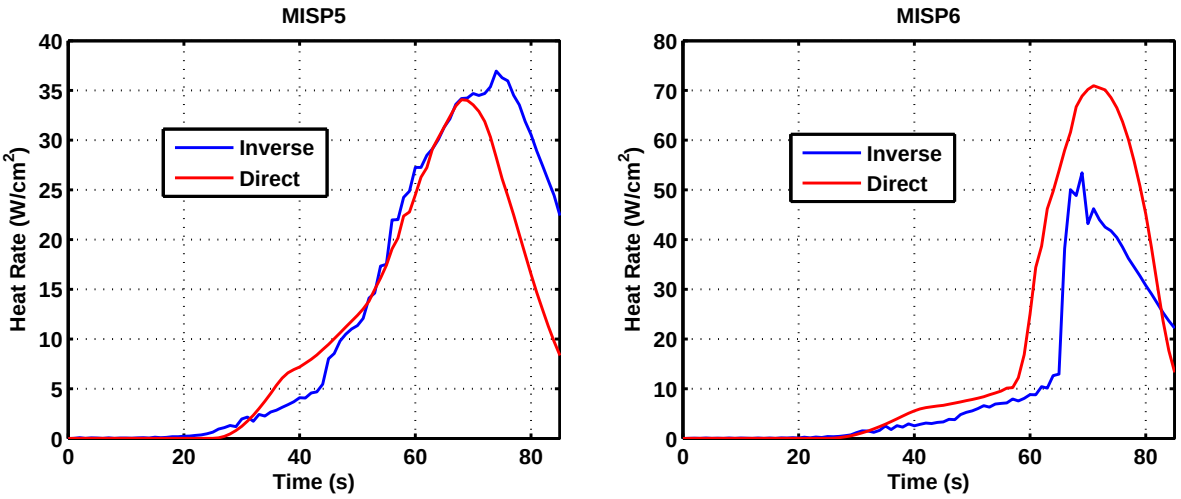

Figure 16. Comparison of the estimated and direct FIAT heating environments for plugs 5 and 6.

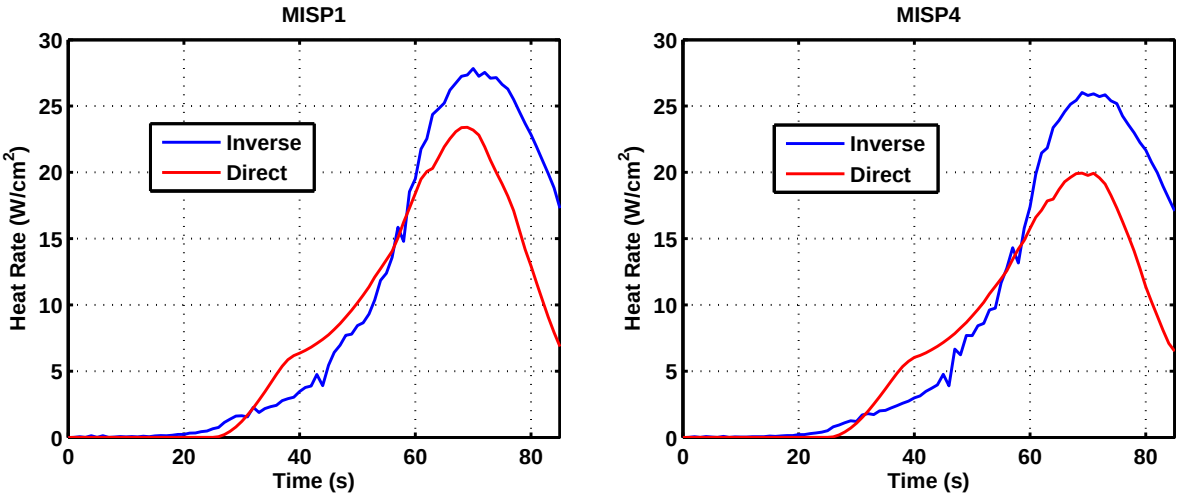

Figure 17. Comparison of the estimated and direct FIAT heating environments for plugs 1 and 4.

on CFD predictions (direct) for all plugs. Surface heating at plug 7 was much higher than expected, while plugs 2, 3 and 6 were lower than predictions. The plugs that remained laminar (1, 4, and 5) had a slightly higher estimated heating than expected. It should be noted again that the surface heat rates provided here are based on FIAT calculations and there is a fundamental difference between FIAT heat rates and CFD heat rates due to the blowing correction and different surface energy balance approaches used. This should be taken into account while comparing these reported numbers with CFD heat rates. The comparisons between CFD and FIAT heat rates presented in the "Direct Analysis" section provide an indication of the range of differences to be expected (see Figures 6 and 7).

Table 3. Inversely estimated peak heat rates compared with direct FIAT heat rates based on CFD predictions.

Peak Heat Rate (W/cm^2)	Plug 1	Plug 2	Plug 3	Plug 4	Plug 5	Plug 6	Plug 7
Direct	23.4	81.4	81.4	20.0	34.2	71.1	28.9
Inverse	28.1	73.1	63.2	26.0	37.0	54.0	54.9

Table 4 shows the turbulent transition times derived from the estimated heating profiles. Due to the lagged nature of heat transfer, these times are about 1 second earlier than the times derived from the subsurface temperature rate profile shown earlier. These values are compared with pre-flight transition predictions based on a momentum thickness Reynolds number threshold of 250. As mentioned before,

turbulent transition was probably induced by roughness and moved very quickly across all the plugs.

Table 4. Inversely estimated transition times compared with CFD predictions based on $Re_\theta = 250$.

Time after Entry (s)	Plug 2	Plug 3	Plug 6	Plug 7
Direct ($Re_\theta = 250$)	56	56	58	70
Inverse	64	63	65	65

Table 5 shows the surface heating augmentation calculated based on the comparison of estimated heat rates over a two-second period after transition. We can see that plugs 2 and 3 experienced the highest augmentation followed by plugs 6 and 7. This trend is expected as the distance from the stagnation point increases from plug 7 located at the apex region to plugs 2 and 3 at the shoulder. Note that these numbers should not be directly compared with turbulent heating augmentation values derived based on comparison of predicted laminar and turbulent heatings at a given time. These ratios are calculated over a two-second time period and they are affected by the rising nature of heat rate over the two-second period.

Table 5. Turbulent heating augmentation over a two-second period derived from estimated surface heating profile.

	Plug 2	Plug3	Plug 6	Plug 7
Heat rate at transition time (W/cm^2)	13.3	12.0	13.1	21.2
Heat rate at 2 seconds after transition time (W/cm^2)	73.1	63.2	51.0	54.7
Heating augmentation (ratio)	5.50	5.27	3.89	2.58

As a final note, the reader should remember that the surface heating reconstruction approach used here was based on the estimation of C_H profile while keeping other parameters constant and using nominal FIAT models in the calculations. The estimation results do not resolve structural uncertainties in these models. In future work, the effect of these uncertainties on the surface heating estimation results will be explored. As an example, it is believed that the equilibrium gas/surface interaction models used in FIAT overpredict recession at low heat rates. Unfortunately today, no validated comprehensive finite-rate model exists for PICA in a CO_2 environment. Furthermore, finite rate models are computationally expensive and require the identification of reaction rates; therefore, application of inverse methods to these models remains a challenge. The authors are currently in the process of developing approximate techniques to enable estimation of surface heating using FIAT while specifying a pre-defined recession profile. This will allow us to explore different limiting cases of recession and estimate surface heating for those cases.

VI. Conclusions

The MSL thermocouple flight data were presented in this paper. The vehicle's aeroheating environment was predicted using the CFD code DPLR and the heatshield temperature at the thermocouple locations was calculated at all MISP plugs using FIAT based on these CFD environments. These model predictions were compared with the flight data. In addition to this direct analysis, the time-dependent surface heating profiles at all plugs were estimated from flight thermocouple data using inverse estimation methods. A close agreement between the model predictions and TC1 flight data was achieved through inverse estimation of the surface heating at all seven plugs.

Turbulent transition at the heatshield shoulder (plugs 2 and 3) happened later than the smooth wall CFD predictions (based on a momentum thickness Reynolds number threshold of 250) and moved rapidly to plugs 6 and 7. This is indicative of a roughness-induced transition. Due to the late turbulent transition, plugs 2, 3 and 6 experienced lower than expected peak heating rates and thermocouple temperatures did not reach the levels predicted by computational models for these plugs. Plugs 1, 4 and 5 remained laminar throughout the entire trajectory and experienced slightly higher peak heating than expected. Possible reasons include lower surface emissivity because of Silica flow on the plugs or radiative heating. Plug 7 experienced higher than expected laminar heating and became turbulent earlier than CFD model predictions. For this reason, the flight temperature data for this plug reached much higher levels than model predictions. It was also observed that the flight TC1 temperature cooled down at a slower rate than model predictions for all plugs. In the inverse analysis, we were not able to match this trend using the C_H estimation approach. Additional analyses will be performed to investigate this behavior further. A TC driver analysis was also performed using

the measurements from TC1 as true boundary conditions and it was observed that FIAT TC2 predictions matched the flight data well while some differences existed in the deeper thermocouples.

Acknowledgments

This work was funded by the NASA grant NNX12AF94A from the NRA Research Opportunities in Aeronautics 2010. Portions of this work were conducted under NASA contract NNA10DE12C to ERC, Incorporated. The authors are grateful to David Saunders for his help with the CFD environments. We also thank Bernie Laub, Karl Edquist, Jose Santos, Michael Wright, Adam Amar, Brandon Oliver and Robin Beck for their time in discussing some aspects of this work.

References

[1]Wright, M., Chun, T., Edquist, K., Hollis, B., Krasa, P., and Campbell, C., "A Review of Aerothermal Modeling for Mars Entry Missions," *48th AIAA Aerospace Sciences Meeting*, No. AIAA 2010-44, January 2010.

[2]Wright, M., Milos, F., and Tran, P., "Afterbody Aeroheating Flight Data for Planetary Probe Thermal Protection System Design," *Journal of Spacecraft and Rockets*, Vol. 43, No. 5, 2006, pp. 929–943.

[3]Ingoldby, R., Michel, F., Flaherty, T., Doryand, M., Preston, B., Villyard, K., and Steele, R., "Entry Data Analysis for Viking Landers 1 and 2 Final Report," Tech. rep., NASA CR-159388, Martin Marietta Corporation, 1976.

[4]Schmitt, D., "Base Heating on a an Aerobraking Oribital Transfer Vehicle," *21st AIAA Aerospace Sciences Meeting*, No. AIAA 83-0408, Reno, Nevada, January 1983.

[5]Edquist, K., Wright, M., and Allen, G., "Viking Afterbody Heating Computations and Comparisons to Flight Data," *44th AIAA Aerospace Sciences Meeting*, No. AIAA 2006-386, Reno, Nevada, January 2006.

[6]Milos, F., Chen, Y., Congdon, W., and Thornton, J., "Mars Pathfinder Entry Temperature Data, Aerothermal Heating, and Heatshield Material Response," *Journal of Spacecraft and Rockets*, Vol. 36, No. 3, 1999, pp. 380–391.

[7]Mahzari, M., Braun, R., and White, T., "Reconstruction of Mars Pathfinder Aerothermal Heating and Heatshield Material Response Using Inverse Methods," *43rd AIAA Thermophysics Conference*, No. AIAA 2012 2872, New Orleans, Louisiana, June 2012.

[8]Steltzner, A., Kipp, D., Chen, A., Burkhart, P., Guernsey, C., Mendeck, G., Mitcheltree, R., Powell, R., Rivellini, T., Martin, A. S., and Way, D., "Mars Science Laboratory entry, descent and landing system," *IEEE Aerospace Conference*, No. IEEAC1497, Big Sky, MT, March 2006.

[9]Tran, H., Johnson, C., Rasky, D., Hui, F., Chen, Y., and Hsu, M., "Phenolic Impregnated Carbon Ablators (PICA) for Discovery Class Mission," *31st AIAA Thermophysics Conference*, No. AIAA 1996-1911, New Orleans, LA, June 1996.

[10]Edquist, K., Dyakonov, A., Wright, M., and Tang, C., "Aerothermodynamic Design of the Mars Science Laboratory Heatshield," *41st AIAA Thermophysics Conference*, No. AIAA 2009-4075, San Antonio, Texas, June 2009.

[11]Beck, R., Driver, D., Wright, M., Laub, B., Hwang, H., Slimko, E., Edquist, K., Sepka, S., Willcockson, W., and Thames, T., "Development of the Mars Science Laboratory Heatshield Thermal Protection System," *41st AIAA Thermophysics Conference*, No. AIAA 2009-4229, San Antonio, Texas, June 2009.

[12]Wright, M., Beck, R., Edquist, K., Driver, D., Sepka, S., Slimko, E., Willcockson, W., DeCaro, A., and Hwang, H., "Sizing and Margins Assessment of the Mars Science Laboratory Aeroshell Thermal Protection System," *41st AIAA Thermophysics Conference*, No. AIAA 2009-4231, San Antonio, Texas, June 2009.

[13]Gazarik, M., Wright, M., Little, A., Cheatwood, F., Herath, J., Munk, M., Novak, F., and Martinez, E., "Overview of the MEDLI Project," *IEEE Aerospace Conference*, No. IEEE 2008-1510, Big Sky, Montana, March 2008.

[14]Wright, M., White, T., and Mangini, N., "Data Parallel Line Relaxation (DPLR) Code User Manual; Acadia-Version 4.01.1," Tech. rep., NASA TM 2009-215388, Oct. 2009.

[15]Chen, Y. and Milos, F., "Ablation and Thermal Response Program for Spacecraft Heatshield Analysis," *Journal of Spacecraft and Rockets*, Vol. 36, No. 3, 1999, pp. 475–483.

[16]Bose, D., White, T., Santos, J., Feldman, J., Mahzari, M., Olson, M., and Laub, B., "Initial Assessment of Mars Science Laboratory Heat Shield Instrumentation and Flight Data," *51st AIAA Aerospace Sciences Meeting*, Dallas, Texas, 2013.

[17]White, T., Cozmuta, I., Santos, J., Laub, B., and Mahzari, M., "Proposed Analysis Process for Mars Science Laboratory Heat Shield Sensor Plug Flight Data," *42nd AIAA Thermophysics Conference*, No. AIAA 2011-3957, Honolulu, Hawaii, June 2011.

[18]Oishi, T., Martinez, E., and Santos, J., "Development and Application of a TPS Ablation Sensor for Flight," *46th AIAA Aerospace Sciences Meeting*, No. AIAA 2008-1219, January 2008.

[19]Santos, J., Jacobs, T., and Martinez, E., "Isotherm Sensor Calibration Program for Mars Science Laboratory Heat Shield Flight Data Analysis," *42nd AIAA Thermophysics Conference*, No. AIAA 2011-3955, Honolulu, Hawaii, June 2011.

[20]Milos, F., "Galileo Probe Heat Shield Ablation Experiment," *31st AIAA Thermophysics Conference*, No. AIAA 1996-1823, New Orleans, LA, June 1996.

[21]Striepe, S., Powell, R., Desai, P., and Queen, E., "Program To Optimize Simulated Trajectories (POST II)," Tech. rep., NASA Internal Document, 2004.

[22]Karlgaard, C., Kutty, P., Schoenenberger, M., Shidner, J., and Munk, M., "Mars Entry Atmospheric Data System Trajectory Reconstruction Algorithms and Flight Results," *51st AIAA Aerospace Sciences Meeting*, Dallas, TX., 2013.

[23]Mitcheltree, R. and Gnoffo, P., "Wake Flow about the Mars Pathfinder Entry Vehicle," *Journal of Spacecraft and Rockets*, Vol. 32, No. 5, 1995, pp. 771–776.

[24]Mitcheltree, R., "Computational Aerothermodynamics for Mars Pathfinder Including Turbulence," No. AIAA 95-3493, August 1995.

[25]Ramshaw, J., "Self-Consistent Effective Binary Diffusion in Multicomponent Gas Mixtures," *Journal of Non-Equilibrium Thermodynamics*, Vol. 15, No. 3, 1990, pp. 295–300.

[26]Baldwin, B. and Lomax, H., "Thin Layer Approximation and Algebraic Model for Separated Turbulent Flows," *16th AIAA Aerospace Sciences Meeting*, No. AIAA 1978-257, Huntsville, AL, January 1978.

[27]Milos, F., Chen, Y., and Gokcen, T., "Nonequilibrium Ablation of Phenolic Impregnated Carbon Ablator," *48th AIAA Aerospace Sciences Meeting*, No. AIAA 2010-981, Orlando, Florida, January 2010.

[28]Ozisik, M. and Orlande, H., *Inverse Heat Transfer: Fundamentals and Applications*, Taylor and Francis, New York, 2000.

[29]Beck, J. and Arnold, K., *Parameter Estimation in Engineering and Science*, Wiley, New York, 1977.

[30]Beck, J., Blackwell, B., and Clair, C. S., *Inverse Heat Conduction, Ill-posed Problems*, Wiley, New York, 1985.

[31]Mahzari, M. and Braun, R., "Time-dependent Estimation of Mars Science Laboratory Surface Heating from Simulated MEDLI Data," *43rd AIAA Thermophysics Conference*, No. AIAA 2012-2871, New Orleans, Louisiana, June 2012.

[32]Woodbury, K., *Inverse Engineering Handbook*, CRC Press, Boca Raton, 2003.

[33]Tikhonov, A. and Arsenin, V., *Solution of Ill-Posed Problems*, Winston and Sons, Washington, DC, 1977.